

Mass Segregation in Young LMC Clusters I. NGC 2157 ¹

Philippe Fischer²³

Dept. of Astronomy, University of Michigan, Ann Arbor, MI 48109

Carlton Pryor

Dept. of Physics & Astronomy, Rutgers, the State University of New Jersey, P.O. Box 849,
Piscataway, NJ 08855-0849

Stephen Murray

Lawrence Livermore National Laboratory, L-023, P.O. Box 808, Livermore, CA 94550

Mario Mateo

Dept. of Astronomy, University of Michigan, Ann Arbor, MI 48109

Tom Richtler

Sternwarte der Universität Bonn, Auf dem Hügel 71, D-53121 Bonn

ABSTRACT

We have carried out WFPC2 *V*- and *I*-band imaging of the young LMC cluster NGC 2157. Construction of a color-magnitude diagram and isochrone fitting yields an age of $\tau = 10^8$ yrs, a reddening $E(B - V) = 0.1$ and a distance modulus of 18.4 mag. Our data covers the mass range $0.75 M_{\odot} \leq m \leq 5.1 M_{\odot}$. We find that the cluster mass function changes significantly from the inner regions to the outer regions, becoming steeper (larger number of low mass stars relative to high mass stars) at larger radii.

The age of NGC 2157 is comparable to its two-body relaxation timescale only in the cluster core. The observed steepening of the mass function at larger radii is therefore most likely an initial condition of the cluster stars. Such initial conditions are predicted in models of cluster star formation in which dissipative processes act more strongly upon more massive stars.

¹Based on observations with the NASA/ESA *Hubble Space Telescope* obtained at the Space Telescope Science Institute, which is operated by the Association of Universities for Research in Astronomy Inc., under NASA contract NAS 5-26555.

²Hubble Fellow

³Visiting Astronomer, National Optical Astronomy Observatories, which is operated by the Association of Universities for Research in Astronomy, Inc., under contract to the National Science Foundation.

1. Introduction

While some progress has been made towards understanding the formation of isolated stars, the formation of star clusters is still poorly understood, even though the majority of stars probably do form in clusters. Until we obtain a better understanding of the physical processes of cluster formation, knowledge of star formation and the spectral, photometric, and chemical evolution of composite stellar systems will remain significantly incomplete.

Obtaining observational constraints for cluster formation theory has been very difficult. Star-forming Galactic clusters are sparse and tend to lie in heavily obscured regions. Older open clusters have relatively few stars and low surface densities; thus, studies are plagued by small number statistics and field star contamination. The globular clusters are all older than 10^{10} yrs; stellar and dynamical evolution have erased most information pertaining to their formation.

In contrast, the massive, young Magellanic Cloud clusters are excellent laboratories for addressing fundamental issues of star formation in cluster environments. They are relatively unobscured, possess rich populations of stars, have high surface densities, and exhibit a large range in main-sequence stellar masses. Their masses and other properties make some of these clusters closely resemble the expected appearance of young Galactic globular clusters, suggesting that these two kinds of clusters formed by similar processes. Because these clusters are younger than their relaxation times (as young as 10^7 yrs) and orbit in the relatively weak gravitational field of the LMC, they have had little dynamical evolution since formation, and so they may be used to infer the conditions present in globular clusters immediately following star formation.

In particular, the lack of extensive two-body relaxation in the LMC clusters makes them good tools for discriminating among different theories of cluster star formation. Several theories differ crucially in whether or not extensive dissipation is present during the cluster star formation process and in the role played by the dissipative process in affecting star formation. The different theories therefore make significantly different predictions for the behavior of the stellar initial mass function as a function of cluster radius, which may be tested by HST observations.

Previous ground-based studies of the outer regions of young LMC clusters (Mateo 1988, Elson et al. 1989a, Lee 1990, Sagar & Richtler 1991, see the review in Mateo 1992) revealed mass functions similar to a Salpeter function in the outer regions, but since the inner regions could not be resolved, mass segregation could not be investigated. More recently, studies of R136 (Hunter et al. 1995) and NGC 1818 (Hunter et al. 1997) with HST have found Salpeter mass functions and little evidence of mass segregation.

To test the cluster formation models we are studying four young LMC clusters using HST WFPC2 data. In this paper we present results for the first cluster, NGC 2157, and

focus on the search for primordial mass segregation in order to help distinguish among the current plethora of cluster formation models and provide strong constraints for subsequent, more detailed, models. Section 2 briefly describes the WFPC2 observations and Sec. 3 discusses the color-magnitude diagrams and isochrone fitting. Section 4 presents the cluster luminosity function and the evidence for radial variation in the mass function. Whether this mass segregation is primordial is discussed in Sec. 6. Section 7 discusses the implications of these results for theoretical models of cluster formation and describes some future plans.

2. Observations

Images of NGC 2157 were taken through two filters with WFPC2 on 9 Dec. 1995. Exposure times were 5×300 s and 2×10 s through F555W and 4×300 s, 1×187.5 s and 1×10 s through F814W. The 187.5s exposure was scheduled for 300s but was aborted due to telescope problems. The cluster center is located in the PC frame. Additional exposures were taken of a field offset $26''$ east and $110''$ north from the cluster field. These consisted of 5×300 s exposures through F555W and 5×300 s exposures through F814W. There was a single integer-pixel dither for each sequence of five 300s exposures.

The images have the normal pipeline preprocessing and the long exposures were combined using the Tukey biweight algorithm (Andrews et al. 1972; see Beers et al. (1990) for an astronomical application), which employs a robust weighting scheme to estimate the mean (the aborted exposure was scaled by 1.6). This technique was very effective at eliminating cosmic rays and no cosmic rays are seen in the final combined images.

3. Photometry and Color-Magnitude Diagrams

We used the profile-fitting photometry package DAOPHOT II (Stetson 1987, Stetson et al. 1990) with variable PSF to obtain stellar photometry for both the cluster and background fields. The photometry from ALLSTAR was aperture corrected to a $0.5''$ radius aperture and the zero points, color terms, and CCD gains from Holtzman et al. (1995) were adopted. We also used the 0.04 mag ramp in the CCD y directions, as suggested by Holtzman et al. (1995), to correct for charge-transfer-efficiency problems. The WFPC2 passbands were transformed to Johnson V and I passbands as specified in Holtzman et al. (1995) with a reddening correction of $E(B - V) = 0.1$ (see below). The estimated uncertainties in the photometric zero points are around 0.05 – 0.10 mag. The reddening corrected photometry data for the cluster fields are tabulated on the AAS CD-ROM Vol. ? as Tables 1 - 4, and the background fields in Tables 5 - 8.

Figure 1 shows the V_0 vs. $(V - I)_0$ color magnitude diagrams (CMDs) for all four WFPC2 fields. The only stars displayed are those detected independently in the two frames and whose

positions, when transformed from one frame to the other, agreed to within 1.0 pixel. Because of saturation on the long-exposure images, the short-exposure photometry was used for all stars with $V_0 < 18.0$.

The CMDs show clear evidence for a mixture of populations; a young population belonging mainly to the cluster (with some LMC field stars mixed in) and an older, evolved stellar sequence belonging exclusively to the LMC field. Fitting $z = 0.008$ isochrones from Bertelli et al. (1994) to the young population yielded $E(B - V) = 0.1$ mag, $\tau = 1 \times 10^8$ yrs, and $(m - M) = 18.4$. The metallicity of NGC 2157 is unknown at this time so we adopt $z=0.008$, which is the approximate mean for the young LMC clusters. We have dereddened the apparent magnitudes using $E(B - V) = 0.1$ and assuming $A_{F555W} = 0.3175$ and $A_{F814} = 0.1895$ (Holtzmann et al. 1995). This reddening is the same as found by Mateo et al. (1990) based on both *BVI* photometry of NGC 2157 Cepheids and comparisons of observed colors of upper main sequence stars with models of high mass stars. Errors in the photometric zero points lead to corresponding errors in the distance modulus and reddening. However, the age determination is less sensitive to the photometric zero points since the age is determined by the difference in brightness between the evolved stars and the strong main sequence kink around $V = 21$.

Figure 2 shows the CMDs of the background fields. These also exhibit a mixture of populations.

4. Luminosity and Mass Functions

The main goal of this paper is to study the stellar mass function of NGC 2157. The first step is to construct a luminosity function (LF hereafter) for the cluster corrected for incompleteness and field star contamination.

4.1. Completeness Corrections

We determined the incompleteness using the recovery of artificial stars added simultaneously to our V and I frames. The frames with added stars are reduced in the same way as the originals. Artificial stars are considered detected only if they are independently found in both bandpasses, as were the real stars. We draw the stars randomly from a power-law mass function and determine the V - and I -band brightnesses using the Bertelli et al. (1994) isochrone with $Z = 0.008$ and $\tau = 1 \times 10^8$ yrs. Stellar positions are randomly drawn from the radial distribution determined from stars with $V > 22.0$ for each CCD image (a uniform distribution was used for the background fields). The input mass function was varied until the recovered LF resembled the measured LF (and hence the input mass function was similar to the cluster mass function). By matching the recovered LF to the cluster LF we

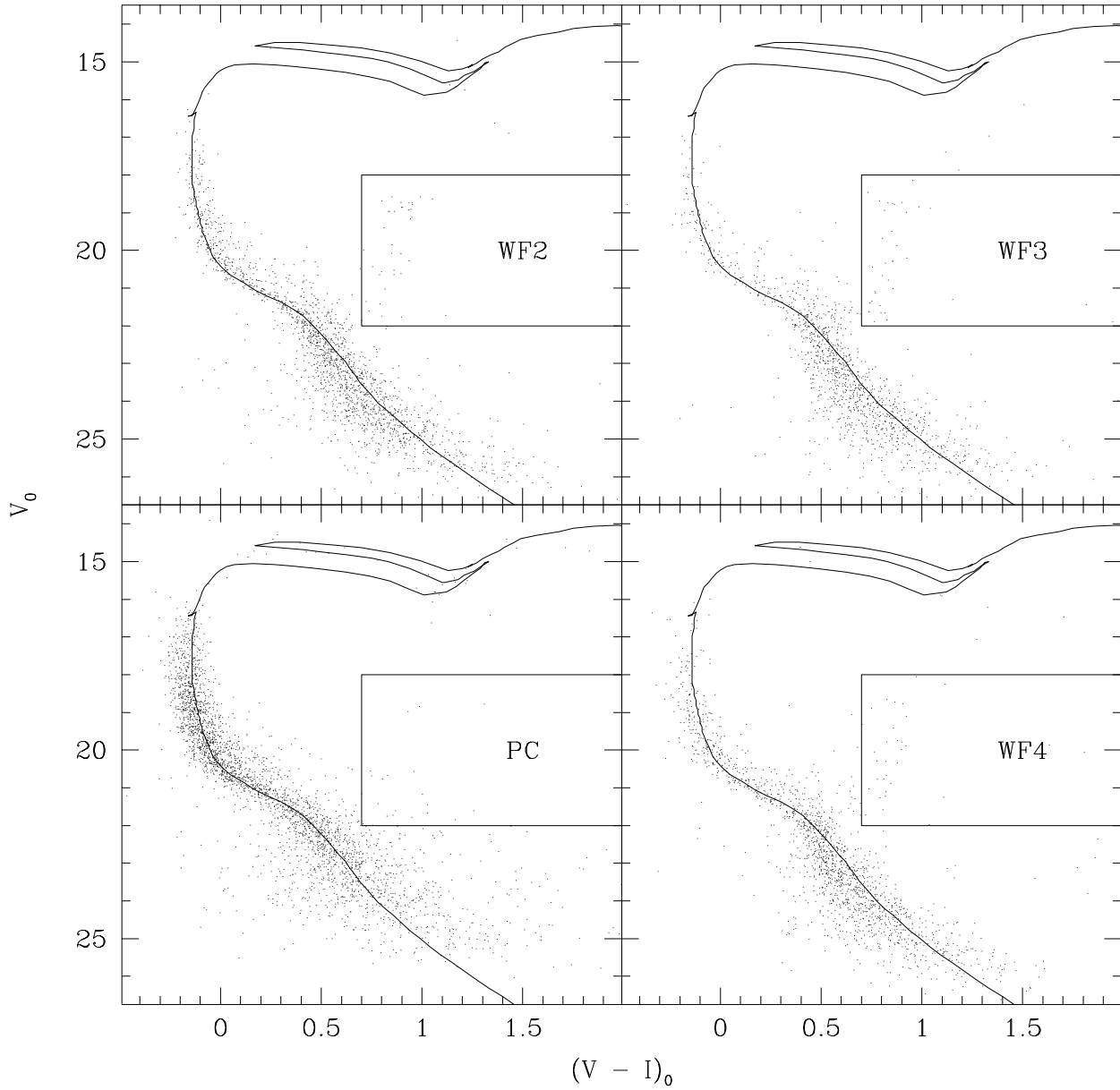


Fig. 1.— V and I color-magnitude diagrams for the field around NGC 2157. The cluster center is located in the PC field. The stellar magnitudes have been dereddened assuming $E(B - V) = 0.1$ mag. The solid line is the Bertelli et al. (1994) isochrone with $\tau = 1 \times 10^8$ yrs and $Z = 0.008$, which fits the data well for the reddening given above and $(m - M) = 18.4$. The boxes contain evolved old stars which belong to the LMC field.

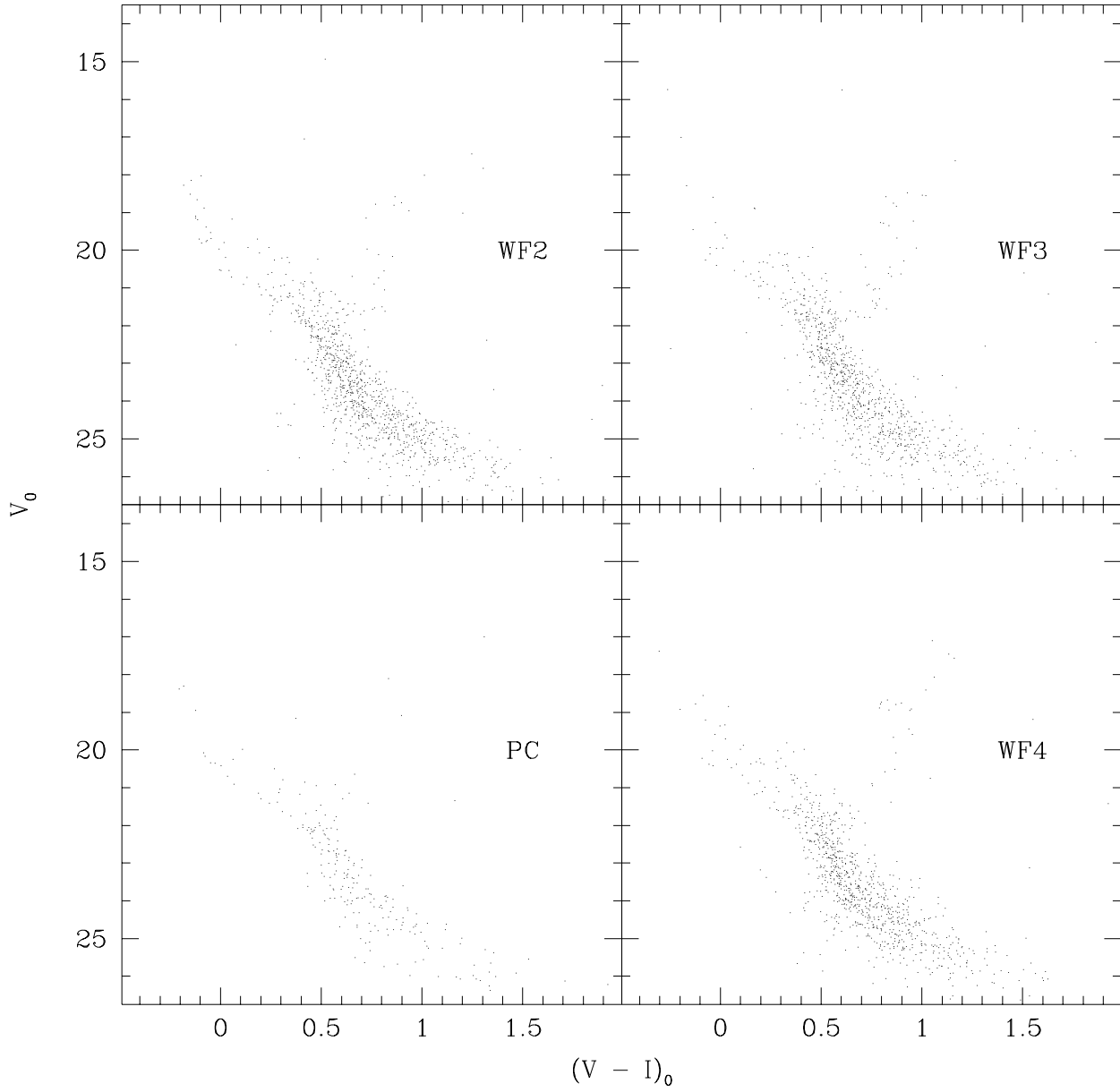


Fig. 2.— V and I color-magnitude diagrams for a field offset $110''$ from NGC 2157. The stellar magnitudes have been dereddened assuming $E(B - V) = 0.1$ mag.

ensure that the simulated data suffer from the same systematic effects as the real data. For example, if some stars, due to blending, are measured too bright, then this should be seen at a similar level in both the simulated and real data. For each WFPC2 image of both the cluster and background fields, we carried out a minimum of 300 simulations, each containing 200 artificial stars. In Fig. 3 we show completeness fraction curves for three different cluster regions (described below) and the background fields. The measured completeness fraction is dependent on position; the regions near the cluster center have substantially lower completeness fractions than regions at larger radii due to crowding. The data were corrected by dividing by the completeness functions in 0.25 magnitude bins.

4.2. Luminosity Functions

The upper two panels of Fig. 4 show the completeness-corrected V - and I -band LFs for the three WFC background fields. Obvious evolved, old stars (located in the box shown in Fig. 1) have been excluded from all background and cluster LFs shown in this paper. The bottom two panels show the *combined* V - and I -band LFs with 1σ error bars determined from

$$\sigma \approx \sqrt{\frac{n_{obs}}{f^2} + \frac{(1-f)n_{obs}^2}{n_{added}f^3}} \quad (1)$$

(Bolte 1989), where n_{obs} is the observed number of stars in the bin, n_{added} is the number of stars with magnitudes in the bin which were added to the images for the artificial star simulations, and f is the completeness fraction of the bin from these simulations. These analytical error bars seem to agree reasonably well with the observed field-to-field scatter in the three background LFs.

Figure 5 shows the completeness-corrected, background-subtracted V - and I -band LFs for the entire PC field, while Fig. 6 shows the combined LFs for all three WFC chips. Based on the Bertelli et al. (1994) models, the mass range represented by these LFs is approximately $0.75 \mathcal{M}_{\odot} \leq m \leq 5.1 \mathcal{M}_{\odot}$.

To get a simple estimate of the mass function implied by our data, we assume that it has the form of a single power-law:

$$\frac{dN}{dm} \propto m^{-(1+x)}, \quad (2)$$

where m is stellar mass, N is number of stars, and $x = 1.3$ corresponds to the Salpeter mass function. We convert this to a luminosity function using the mass-luminosity relationship in Bertelli et al. (1994) and compare it to the measured luminosity function. The power-law exponents that best fit the V - and I -band LFs for the PC chip are $x_V = 0.95_{-0.25}^{+0.30}$ and $x_I = 1.0_{-0.30}^{+0.25}$, where the quoted uncertainties are the 95% upper and lower bounds. The reduced chi-square values for the fits are $\chi_{\nu}^2 = 1.25$ ($\nu = 35$) and $\chi_{\nu}^2 = 1.69$ ($\nu = 31$),

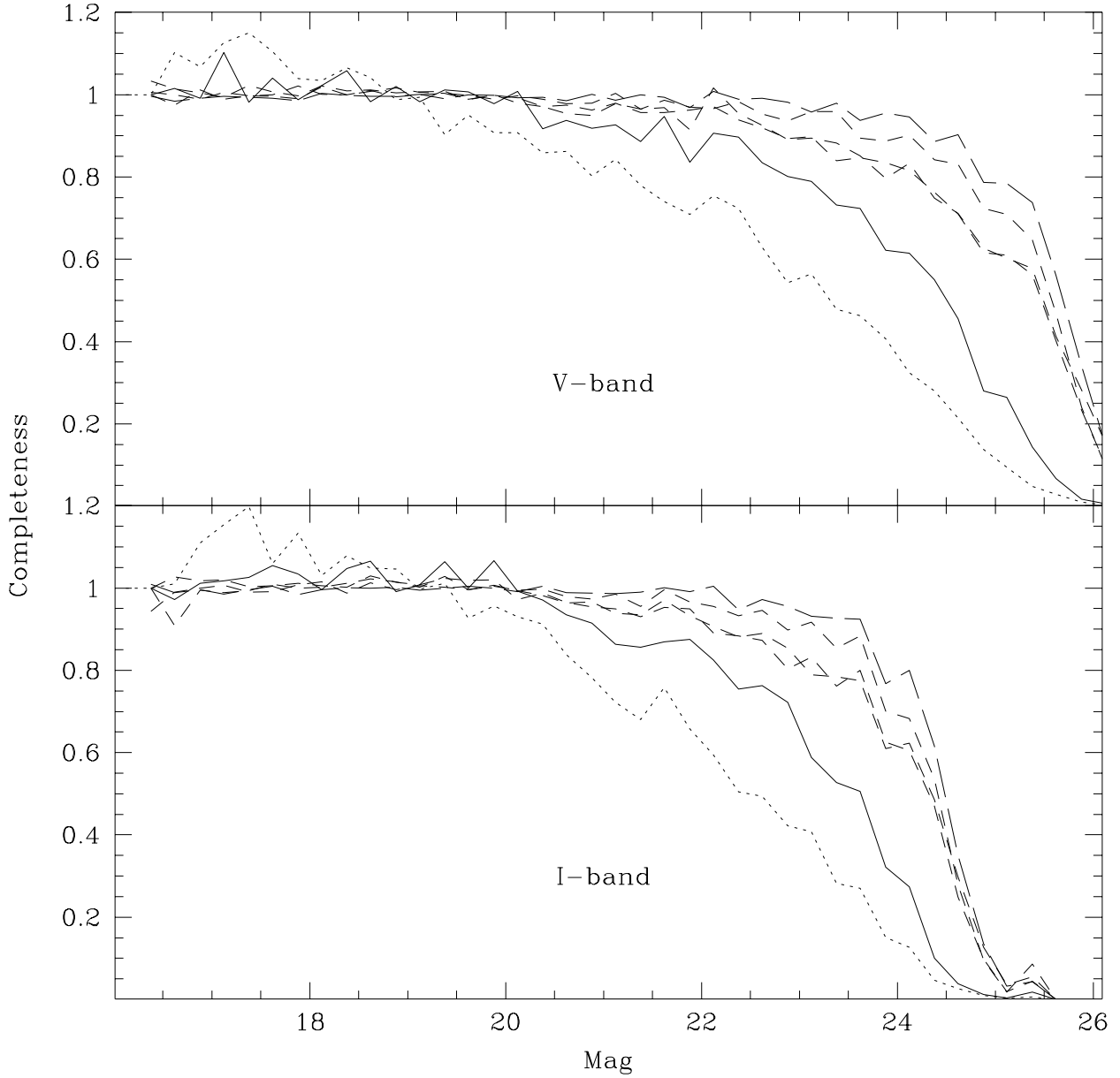


Fig. 3.— Completeness fractions as a function of magnitude derived from artificial star simulations for three different ranges of cluster radii. The dotted line is the small-radius region ($R < 11.8''$; $\bar{R} = 7.5''$), the solid line is the intermediate-radius region (stars on the PC chip with $R \geq 12.3''$; $\bar{R} = 15.7''$), and the short-dashed lines are for the three WF chips ($17.5 \leq R \leq 130''$; $\bar{R} = 59.4$). The long-dashed line show the average completeness curves for the three WF background fields. Stellar magnitudes have been dereddened assuming $E(B - V) = 0.1$ mag

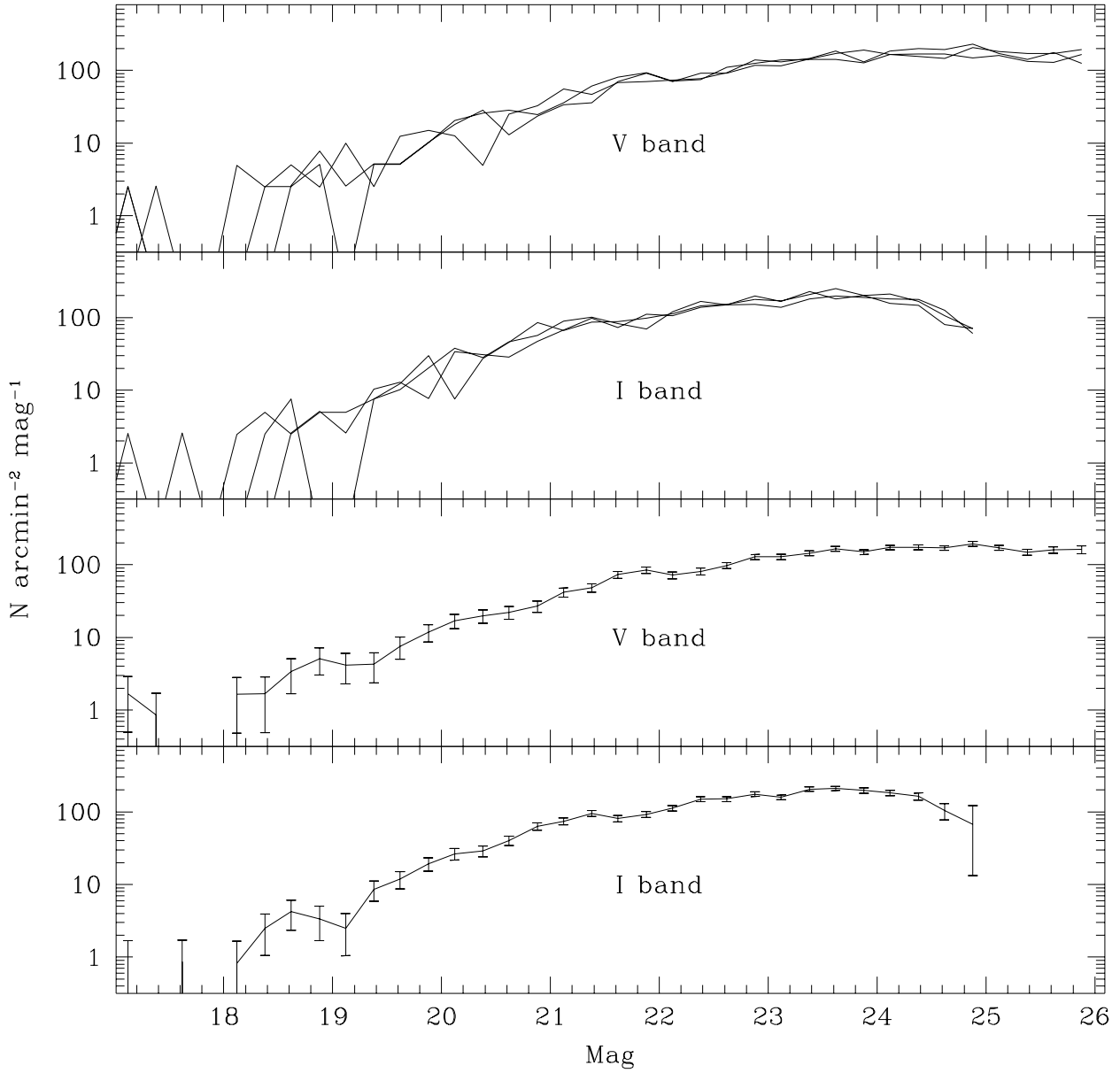


Fig. 4.— The upper two panels show incompleteness-corrected, luminosity functions for the three background WF images. The bottom two panels show the combined luminosity functions, where the error bars are based on eq. 1. The stellar magnitudes have been dereddened by $E(B - V) = 0.1$.

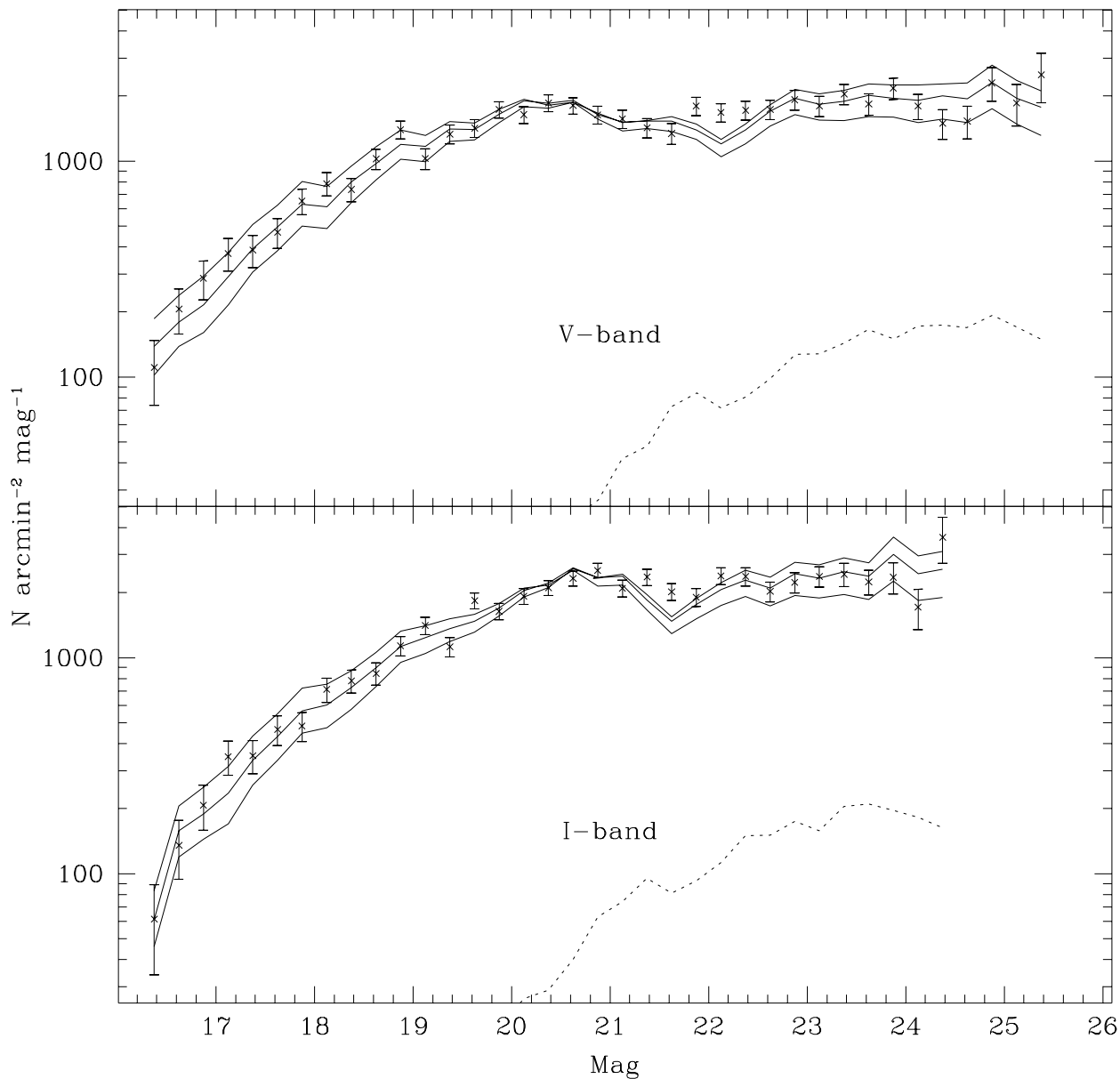


Fig. 5.— *V*- and *I*-band, completeness-corrected, background-subtracted luminosity functions for the PC field (which contains the cluster center). The solid lines are synthetic luminosity functions corresponding to mass functions having $x = 0.70, 1.00,$ and 1.25 . The dashed lines show the background counts. The stellar magnitudes have been dereddened by $E(B - V) = 0.1$.

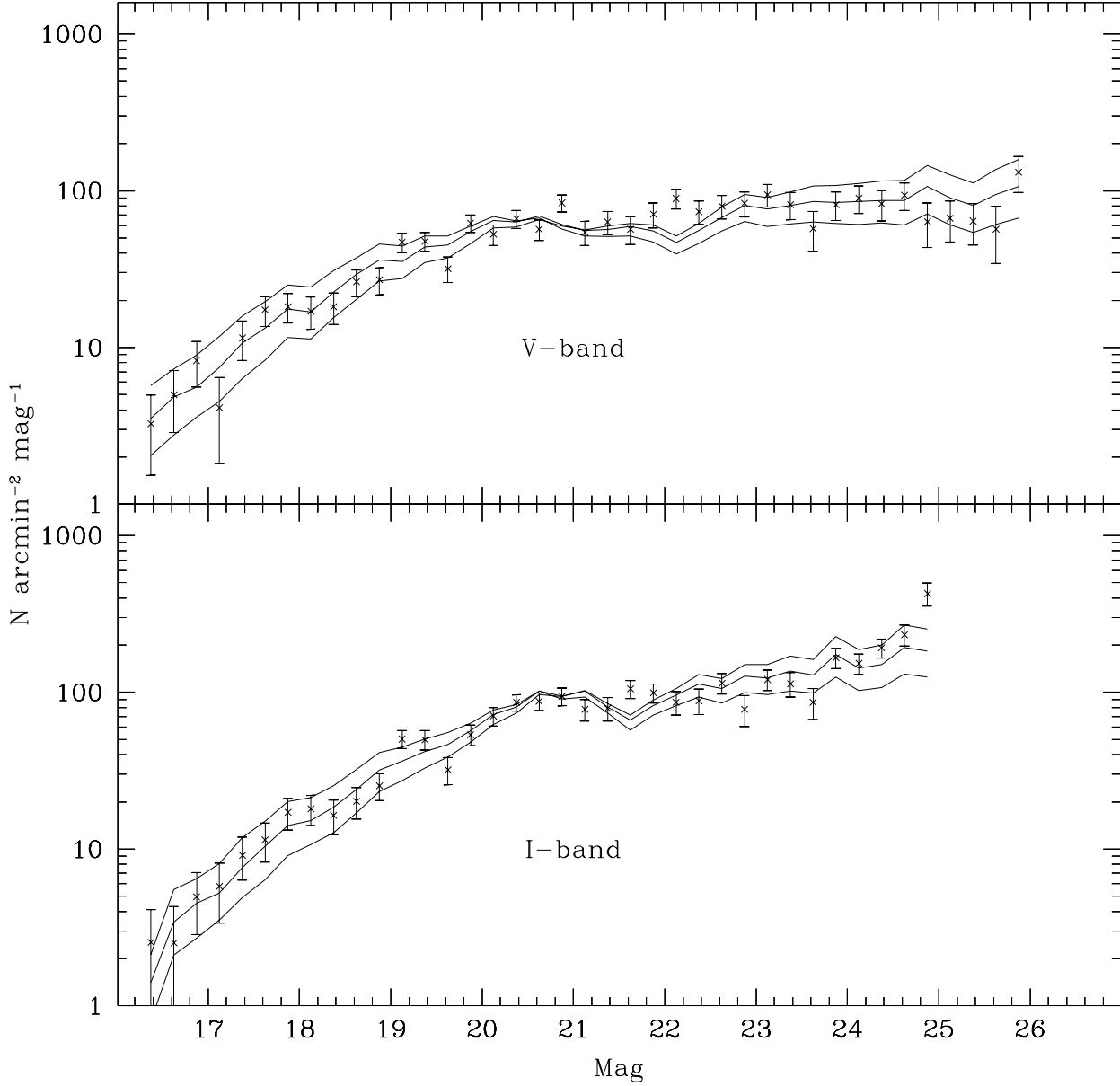


Fig. 6.— Combined V - and I -band, completeness-corrected, background-subtracted luminosity functions for the three WF frames. The solid lines are synthetic luminosity functions corresponding to mass functions with $x = 0.85, 1.30,$ and 1.85 for the V -band data and $x = 1.10, 1.50,$ and 1.90 for the I -band data. The dashed lines show the background counts. The stellar magnitudes have been dereddened by $E(B - V) = 0.1$.

respectively. The probability of seeing chi-square values that large or larger by chance is $P(\chi^2) = 0.14$ for the V -band data and $P(\chi^2) = 0.0087$ for the I -band data. This is marginal evidence for the mass functions differing from pure power laws. However, we have plotted synthetic LFs in Fig. 5 on top of the measured LFs and the agreement appears good. The largest discrepancies appear around $V = 22$ and $I = 21.5$ and these look like a small problem with the mass-luminosity relation. This slope is shallower than, but consistent with, the mass function slope seen in the WFPC2 study of the young LMC cluster NGC 1818 ($x = 1.23 \pm 0.08$, Hunter et al. 1997).

It is worth briefly noting that the mass function slope derived here assumes that the fraction of binary stars in the cluster is zero. If the binary fraction is non-zero, our mass function slope will tend to be too shallow (Sagar & Richtler 1991). Lacking further information regarding the binary fraction, we assume it is zero for the rest of this paper.

4.3. Mass Segregation

To test for a variation of the mass function with projected distance from the cluster center we divide our data set into three: a small-radius sample ($R < 11.8''$, $\bar{R} = 7.5''$), an intermediate-radius sample (stars on the PC chip with $R \geq 12.3''$; $\bar{R} = 15.7''$), and a large-radius sample (all of the stars on the WFC chips, $17.5'' \leq R \leq 130''$; $\bar{R} = 59.4''$). Figure 7 shows the V - and I -band LFs for these three regions and they are tabulated in Table 9. The best-fitting exponents for the different regions are tabulated in Table 10. If we remove the faintest (and most discrepant) point from the I -band LF for the large-radius sample, we get the same value for the mass function exponent, but the chi-square decreases to $\chi^2_V = 1.52$. There appears to be a trend towards steeper mass functions with increasing radius. However, some of the fits to a power-law form are poor, particularly at larger radii. In order to quantify the significance of the radial trend in the LF we carry out two model-independent comparisons.

First we employ a chi-square test between pairs of the LFs. One luminosity function is optimally scaled (so as to minimize chi-square) and chi-square is determined by summing the square of the differences in LFs divided by the uncertainty over all the bins:

$$\chi_{ij}^2 = \sum_{k=1}^n \frac{(s_{ij}b_{i,k} - b_{j,k})^2}{s_{ij}^2\sigma_{i,k}^2 + \sigma_{j,k}^2}. \quad (3)$$

Here $b_{i,k}$ is the k^{th} bin for region i , $\sigma_{i,k}$ is the uncertainty in that bin, n is the number of points and s_{ij} is the scaling factor which minimizes χ_{ij}^2 . The results of the χ^2 tests between the different regions are summarized in Table 11 for different limiting magnitudes (which are given in columns 2 and 6). Columns 3 and 7 have the reduced χ^2 and columns 4 and 8 are the degrees of freedom. Columns 5 and 9 show the probability of exceeding the observed χ^2 value

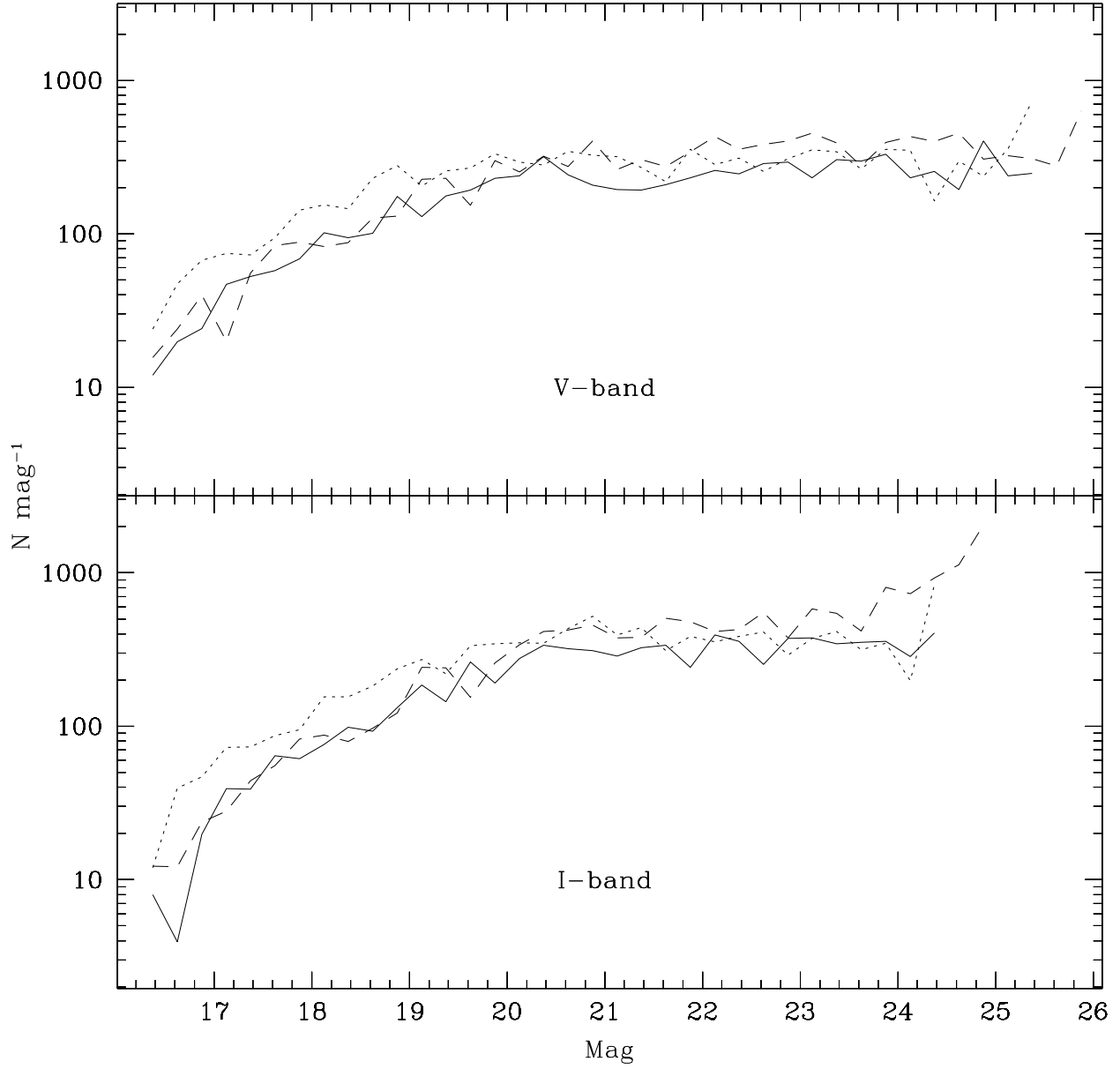


Fig. 7.— Combined V - and I -band, completeness-corrected, background-subtracted luminosity functions for the three radial regions described in the text. The dotted line is the small-radius region, the solid line is the intermediate-radius region and the dashed line is the large-radius region.

by chance. The most significant differences occur between the inner and outer regions for both bandpasses and all values of the limiting magnitude. The differences between the inner and intermediate samples and the intermediate and outer samples are not as significant.

The chi-square test does not fully take into account the information in the systematic variation of the difference between two LFs from positive to negative if they have different average exponents. Therefore the test will tend to underestimate the significance of the differences in cases where the LFs differ systematically. A Kolmogorov-Smirnov (KS hereafter) statistic applied to the two cumulative LFs does use this information and should provide a more sensitive test for differences between the LFs. The difficulty with this approach is that the corrections for incompleteness and the background require that the confidence levels on this KS statistic be determined through Monte Carlo simulations (see Papenhausen 1994, for example).

For each of the radial samples we construct a normalized, background-corrected cumulative luminosity function (CLF hereafter) that steps upwards by

$$\frac{f_i^{-1}}{\sum_{cl} f_i^{-1} - A \sum_{bkgd} f_j^{-1}} \quad (4)$$

at the magnitude of each star in the radial sample of the cluster field and steps downward by

$$\frac{A f_j^{-1}}{\sum_{cl} f_i^{-1} - A \sum_{bkgd} f_j^{-1}} \quad (5)$$

at the magnitude of each star in the background field. Here f_i is the completeness fraction at the magnitude of star i in the specific radial region of the cluster field, f_j is the completeness fraction at the magnitude of star j in the background field, and A is the area of the radial region divided by the area of the background field. The values of the f 's used are those shown in Fig. 3. The KS statistic is the maximum vertical separation between the two CLFs.

The three panels of Fig. 8 show the V -band CLFs for the three pairings of the three radial regions. The samples have been truncated at a limiting magnitude of $V = 24$, where the inner, intermediate, and outer radial samples are about 40%, 60%, and 80% complete, respectively. The vertical lines in the figures mark the position of the largest vertical separation between the two CLFs. In all three panels, the CLF for the inner of the two radial samples rises more quickly at bright magnitudes, signifying a shallower luminosity function at smaller radii. This is the case for every limiting magnitude tried: $V = 25, 24, 23$, and 22 . The I -band CLFs look similar to those for the V -band. Again, the shallower LFs occur at smaller radii for limiting magnitudes of $I = 24, 23, 22$, and 21 . The I -band LFs for the inner, intermediate, and outer regions are about 40%, 70%, and 90% complete at $I = 23$.

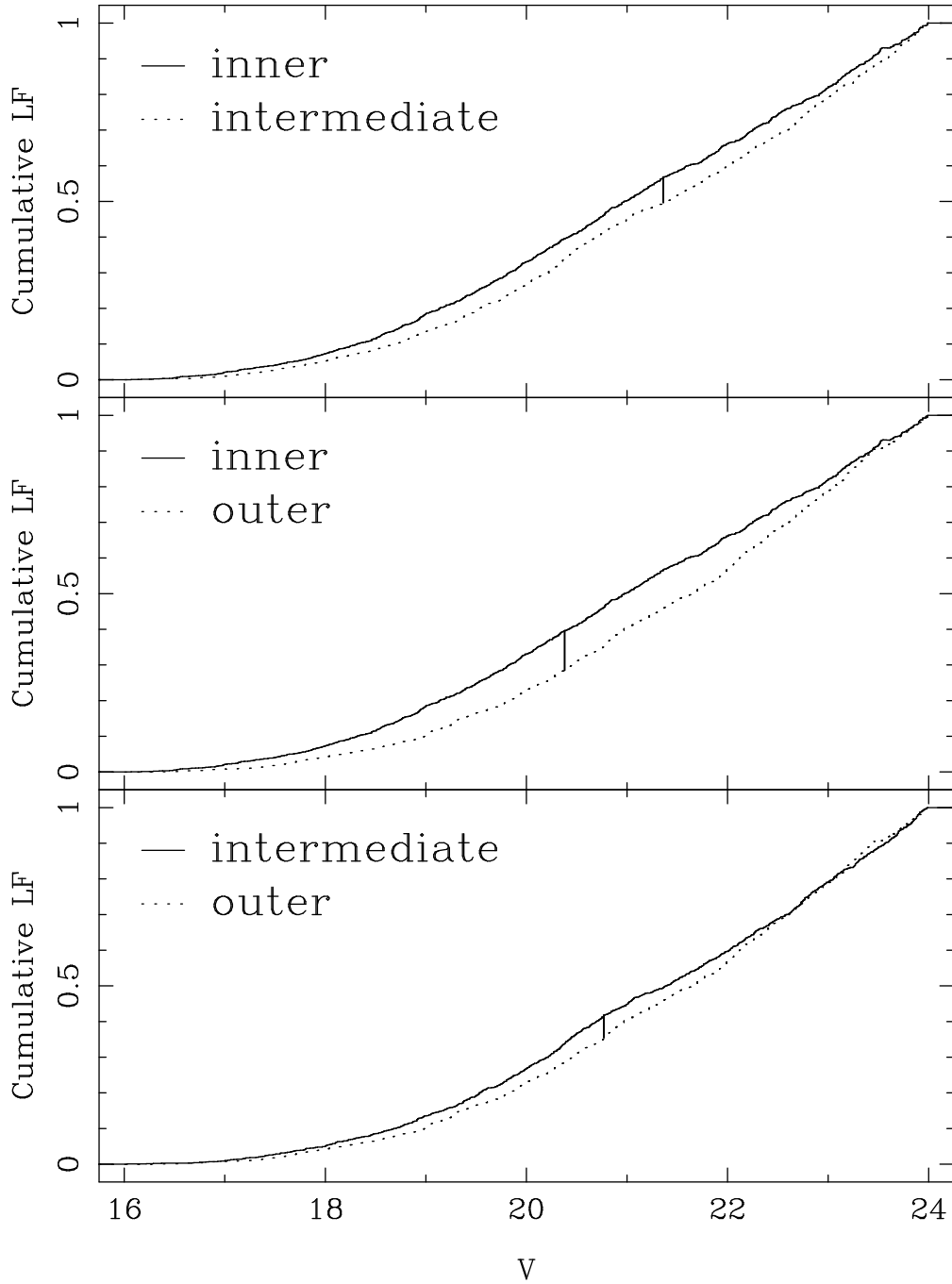


Fig. 8.— Comparisons between pairs of completeness-corrected, background-subtracted, normalized cumulative luminosity functions for different radial regions. The vertical line marks the maximum vertical separation.

We have performed Monte-Carlo simulations to determine if the differences seen in Fig. 8 are significant. The average of the incompleteness-corrected, background-subtracted LFs of the two regions, weighting by the incompleteness-corrected number of stars, is the LF that we use to test the null hypothesis that the two LFs are identical. For each sample, this LF is modified by incompleteness and the background is added to produce “observed LFs” from which two samples of the observed size are drawn. A background sample with the same size as the real background sample is drawn from the real sample with replacement. We calculate the KS statistic for these artificial data and repeat the process 10,000 times. If the number of times that the statistic exceeds the value actually observed is small, the null hypothesis can be rejected.

Table 12 gives the observed KS statistic and the fraction of the simulations for which the statistic exceeded this value for the three pairings of the radial regions. The leftmost column gives the regions compared and is followed by two blocks of seven columns giving numbers for the V -band and I -band LFs. These seven columns are the limiting magnitude, the numbers of stars in the inner, outer, and background samples, the maximum vertical separation between the two LFs, the magnitude at which this occurs, and the fraction of the simulations with a larger maximum vertical separation than was actually observed. Our Monte-Carlo simulations do not include the effect of the uncertainties in the incompleteness corrections, but we present the results for a selection of limiting magnitudes. For the brighter limits, corrections for incompleteness have had little effect on the LFs. The confidence with which the hypothesis of identical LFs can be rejected varies little with limiting magnitude, except to become somewhat less certain at the brightest magnitudes. This is expected because of the smaller sample sizes and the shrinking range of luminosities.

Identical luminosity functions for the inner and outer radial regions can be rejected at better than 99% confidence for nearly all of the limiting magnitudes. Similarly, the LFs of the inner and intermediate regions are different with better than (usually much better than) 95% confidence. The difference between the intermediate and outer region LFs are not significant.

Our detection of mass segregation in NGC 2157 differs from what was found in the $\tau = 20$ Myr LMC cluster NGC 1818 by Hunter et al. (1997). Stars in their PC field, centered on the cluster, yielded $x = 1.21 \pm 0.10$, while the stars in their WFC fields yielded $x = 1.25 \pm 0.08$. Similarly, the very dense, $\tau = 3$ Myr LMC cluster R136 shows no mass segregation, except perhaps within a radius of 0.4 pc (Hunter et al. 1995). We thus turn to a discussion of the possible cause of our observed mass segregation.

5. Mass Segregation: Primordial or Evolutionary?

5.1. Evolution of Mass Segregation: Theory

The first step in deciding whether the mass segregation described in the previous section is primordial is to estimate the relaxation time at different points in the cluster. While theory and simulations show that complete energy equipartition is unlikely to be established in a star cluster (Spitzer 1969, Inagaki & Saslaw 1985, see the summary in Meylan & Heggie 1997), mass segregation certainly does develop on the timescale to exchange energy between stars of different mass by small-angle scattering, t_{eq} . If all of the stars in a cluster begin with the same spatial distribution stars of mass m_1 will at least initially have $t_{eq,1} = (\langle m \rangle / m_1) t_r$, where t_r is the local two-body relaxation time (Spitzer 1969). Thus, mass segregation will be most rapid for the most massive stars and where t_r is shortest (at the smallest radii).

Numerical simulations with a range of stellar masses (*e.g.* Inagaki & Saslaw 1985; Chernoff & Weinberg 1990) do show the profiles of the heaviest stars changing quickest and the effects of segregation propagating outward through the cluster. If stars with different masses start with the same velocity dispersion, the “cooling” of the heavy stars at small radii can leave a kink in their radial density profile (see Fig. 2 of Inagaki & Saslaw 1985, for example). The simulations show that significant mass segregation among the heaviest stars in the core occurs in the local relaxation time, t_{r0} , but affecting a large fraction of the mass of the cluster requires a time comparable to the average relaxation time averaged over the inner half of the mass, t_{rh} .

5.2. Relaxation Timescales for NGC 2157

We will estimate the relaxation times in NGC 2157 from its current density profile, but we point out that the profile may have been different in the past. The rapid loss of mass due to the evolution of massive stars can cause a cluster to expand (Angeletti & Giannone 1979, Chernoff & Weinberg 1990). Observational support for this idea is provided by an apparent increase in the upper limit to the core radii of LMC clusters with age (Elson et al. 1989b). Thus, it is possible that NGC 2157 was denser and had shorter relaxation times when it formed than it does today. However, this same expansion of the core acts to reduce, though not eliminate, mass segregation by expanding the spatial distribution of the heavy stars in the core. Detailed simulations will probably eventually be required to estimate how these processes have affected NGC 2157.

Elson (1991) gives a surface brightness profile for NGC 2157 derived from V and B CCD images. These yielded King-model core radii, r_c , of $9.6'' \pm 1.3''$ and $9.2'' \pm 0.8''$, respectively, which became $8.6''$ and $7.9''$ after being corrected for the seeing.

We performed surface photometry on a 400 s V-band image obtained with the CTIO 0.9 m telescope by PF on January 23, 1995. The stellar images had a full width at half-maximum of $2.0''$. We found the center of the cluster using mirrored autocorrelation (Djorgovski 1987,

Hertz & Grindlay 1985) in a box with sides of $40''$. Table 13 gives the surface brightness profile calculated in circular annuli about this center. From left to right, the columns are the base-10 logarithm of the radius in arcseconds, the surface brightness in V magnitudes per square arcsecond, and the uncertainty in the surface brightness calculated from the scatter between the octants. The photometric calibration is based on V magnitudes from Elson (1991) for stars in the image.

The profile in Table 13 resembles that of Elson (1991) in having a “shoulder” at a radius of about $5''$, but this shoulder is less prominent in our data, presumably because of a slightly different center. A profile calculated from the stars detected in the PC image (but not corrected for incompleteness) shows no shoulder, suggesting that its presence in the surface brightness profiles is due to noise. This eliminates one potential piece of evidence for a lack of relaxation in the core.

The single-component King (1966) model plus a background that best fits the profile in Table 13 has $r_c = 8.7'' \pm 0.6''$, a central surface brightness of $\mu_{0,V} = 17.27 \pm 0.11$ mag arcsec $^{-2}$, a concentration of $c \equiv \log(r_c/r_t) = 1.1 \pm 0.1$, and a background of 20.16 ± 0.005 mag arcsec $^{-2}$. This core radius is very similar to that found by Elson (1991), so we adopt $r_c = 8.7''$ for the remainder of this paper. (This “core radius” is where the surface brightness falls to half of its central value. The King-model scale radius is about 10% larger.)

To estimate relaxation times we also need a mass for NGC 2157. One way to proceed is to combine our luminosity functions with the above King model fit. The luminosity function for the innermost region from Fig. 7 implies a total of 2280 stars with $r < 11.8''$ and masses between $0.75 \mathcal{M}_\odot$ and $5.1 \mathcal{M}_\odot$. With our fitted value for the core radius and our adopted distance of 48 kpc to NGC 2157, $r_c = 2.0$ pc and the central density of stars with masses between $0.75 \mathcal{M}_\odot$ and $5.1 \mathcal{M}_\odot$ is $n_0(0.75, 5.1) = 78$ stars pc $^{-3}$.

If we adopt a mass function power-law exponent of 1.0, which is close to the average for all of our data, then the central mass density of observed stars is $\rho_0(0.75, 5.1) = 130 \mathcal{M}_\odot$ pc $^{-3}$. Assuming that stars with initial masses between 5.1 and $8 \mathcal{M}_\odot$ form $1.0 \mathcal{M}_\odot$ white dwarfs and that stars between 8 and $80 \mathcal{M}_\odot$ form $1.4 \mathcal{M}_\odot$ neutron stars (all of which are retained in the cluster) adds only another $16 \mathcal{M}_\odot$ pc $^{-3}$ to the central density if the same exponent held above the present-day turnoff. Now there must be at least some stars fainter than we observe. If we extrapolate the same power-law mass function to lower masses, then the density in main sequence stars is, for example, $\rho_0(0.1, 5.1) = 270 \mathcal{M}_\odot$ pc $^{-3}$ or $\rho_0(0.03, 5.1) = 350 \mathcal{M}_\odot$ pc $^{-3}$.

If the lower cut-off of the mass function is $0.1 \mathcal{M}_\odot$, then $\rho_0 = 290 \mathcal{M}_\odot$ pc $^{-3}$ and the mean stellar mass is $\langle m \rangle = 0.45 \mathcal{M}_\odot$. With these numbers, the best-fitting King model described above yields a total mass for the cluster of $\mathcal{M} = 4.4 \times 10^4 \mathcal{M}_\odot$, a central relaxation time of $t_{r,0} = 9.1 \times 10^7$ yrs, and $t_{rh} = 9.8 \times 10^8$ yrs. Over the range of King models with acceptable fits to the surface brightness profile, $t_{r,0}$ varies by $\times 4.6$ and t_{rh} by $\times 1.5$.

Clearly, it is desirable to have some check on the extrapolation of the mass function made

above. Observations with the Rutgers Fabry-Perot on the CTIO 4 m telescope have yielded radial velocities for 70 stars in NGC 2157. These data will be presented in more detail elsewhere, however, we use them here to provide a check on our relaxation times. Fitting these data with the $c = 1.1$ King model yields $\rho_0 = 470 \mathcal{M}_\odot \text{pc}^{-3}$, $\mathcal{M} = 7.2 \times 10^4 \mathcal{M}_\odot$, $t_{r,0} = 1.4 \times 10^8 \text{ yrs}$, and $t_{rh} = 1.2 \times 10^9 \text{ yrs}$. While the effect of the velocity measurement errors on the dispersion are removed by our fitting procedure (see Pryor et al. 1989 for more details), the dispersion might still have been inflated by the orbital motions of binary stars, for example. The truth is likely somewhere between the two sets of values.

5.3. Interpretation

Thus, the $1 \times 10^8 \text{ yr}$ age of NGC 2157 is comparable to its $t_{r,0}$ and about a tenth of its t_{rh} . If these times have not been much shorter over most of the age of the cluster, then we expect only a small amount of mass segregation to have occurred in the cluster and it should not extend much beyond the core. If the initial mass function was a power law with exponent 1.0 and extended up to $80 \mathcal{M}_\odot$, then stellar evolution has caused the cluster to lose about half of its mass. This would lead to significant cluster expansion, but the amount of mass loss is sensitive to the adopted upper cutoff and the assumption of a constant exponent. In our galaxy, the initial mass function has an exponent of about 1.6 at large mass (*e.g.*, Basu & Rana 1992). Also, much of the stellar mass loss would occur very early, so any dense initial stage should be short-lived. More definitive statements will require detailed modeling of the dynamical evolution of the cluster, but we conclude that it is unlikely that significant mass segregation has occurred outside of the core since NGC 2157 formed.

6. Discussion

The nature and degree of primordial mass segregation in a star cluster is determined by the importance of interactions during the star formation process in clusters. Different theories which have been proposed to explain cluster star formation lead to very different predictions for primordial mass segregation.

In the classic picture of star formation (Shu et al. 1987), protostars evolve in isolation. Initial objects having masses in excess of M_G (the critical mass for gravitational collapse) form protostellar cores, which accrete gas until infall is halted by winds, which are assumed to result from the onset of deuterium burning. Interactions among the protostellar cores are assumed to be unimportant. The initial evolution of the cluster therefore occurs by violent relaxation and so no mass segregation is expected (Lynden-Bell 1967).

The results are quite similar in the picture of Burkert et al. (1993). In their model, an initial generation of massive stars enriches a primordial gas cloud. Stellar winds and

supernovae lead to expansion of the cloud, which then undergoes star formation, and, subsequently, violent relaxation.

In other models of cluster star formation, interactions among the protostellar cores play a crucial role in the star formation process. The nature of the mass segregation to be expected is determined by whether or not interactions act to enhance or to halt the accretion process.

Podsiadlowski & Price (1992) propose a picture in which the initial stages of star formation closely resemble the picture of Shu et al. (1987). In their model, however, accretion onto a protostellar core is terminated when the infalling gas cloud is disrupted by a close encounter with another protostellar core. Primordial mass segregation in this model results from the changing ratio of the timescales for protostellar collisions and of gas infall onto the protostars. For example, if the gas and protostars in a cluster both follow isothermal density distributions as a function of cluster radius, then

$$\tau_{\text{coll}}/\tau_{\text{infall}} \propto R, \quad (6)$$

where R is the radius within the cluster. The increase of the ratio with R implies that accretion can proceed further for protostellar cores at larger cluster radii, leading to the formation of more massive stars. In this model, therefore, primordial mass segregation is expected in the sense that the IMF should become shallower (have more massive stars) at larger radii.

The exact reverse is expected if encounters *enhance* mass accretion. In the picture of Murray & Lin (1993, 1996), the fragmentation of a protocluster cloud is triggered by thermal followed by dynamical instability. Thermal instability is governed by local heating and cooling balance, and so has no preferred scale length, while the dynamical instabilities involved act preferentially upon smaller scale lengths. The result is therefore a cluster of non-self-gravitating cloudlets. The cloudlets cannot contract individually until their masses exceed M_G , but the cluster as a whole does contract due to the mutual gravity of the cloudlets. As the cloud contracts, mergers among the cloudlets eventually lead to their masses exceeding M_G , at which point they contract to form protostars. Continued encounters can increase the protostellar mass above M_G . The mergers lead to extensive dissipation of kinetic energy. More massive stars undergo more mergers, and so dissipate more energy. They also tend to form near the cluster center, where the density and, hence, the encounter rate are highest. Primordial mass segregation is therefore expected in the sense that the IMF should become steeper (contain a greater fraction of low mass stars) at larger cluster radii.

This last scenario appears to be the most consistent with our observations. We have detected mass segregation in the young LMC cluster NGC 2157 at a high level of confidence. It appears that the relative number of low to high mass stars is an increasing function of radius. Although the results of observations of other clusters is needed to strengthen any conclusions, it is of interest to compare the observations of NGC 2157 with the results of

Murray & Lin (1996). The mass function slopes found for NGC 2157 ($x \approx 1$), and the relatively weak change in the mass function with cluster radius are best represented by models in which the initial mass of the cloudlets, M , is a large fraction of M_G , and in which the initial ratio of the kinetic to potential energy of the cluster $Q = 0.01$ ($Q = 0.5$ in a virialized cluster). In these models, only one or two mergers are required before the onset of protostellar collapse. The population of cloudlets is therefore depleted relatively early in the collapse of the cluster, before the density reaches its peak. Fewer high mass stars are formed, and violent relaxation plays a greater role than in models in which the initial cloudlet mass was a smaller fraction of M_G , for which protostar formation was delayed until later in the collapse. More extensive mass segregation is also seen in models in which $Q = 0.5$.

7. Conclusions and Future Work

Based on WFPC2 imaging of the young LMC cluster NGC 2157 we have detected evidence for mass segregation in the sense of a steeper mass function at larger radius. An analysis of the two-body relaxation times indicates that this mass segregation is most likely mainly primordial and not evolutionary. If it is indeed primordial, then models of cluster formation in which encounters between protostars enhance mass accretion (Murray & Lin 1993, Murray & Lin 1996) are favored while models where encounters halt mass accretion are ruled out.

However, studies of two other young LMC clusters did not find evidence for mass segregation (Hunter et al. 1995, Hunter et al. 1997). We have additional WFPC2 data for two other such clusters, NGC 2004 and NGC 2031, as well as scheduled observations for NGC 1711. We will carry out similar analyses of these clusters in order to better understand our result for NGC 2157. NGC 2004 and NGC 1711 will be particularly interesting as they are even younger than NGC 2157 and therefore evolutionary mass segregation has had less time to operate.

Support for this work was provided by NASA through grants #HF-01069.01-94A and #GO-05904.01-94A from the Space Telescope Science Institute, which is operated by the Association of Universities for Research in Astronomy Inc., under NASA contract NAS5-26555. We thank Karl Gebhardt for analyzing the NGC 2157 Fabry-Perot data.

REFERENCES

- Angeletti, L. & Giannone, P. 1979, *A&A*, 85, 113
 Andrews, D. F., Bickel, P. J., Hampel, F. R., Rogers, W. H., & Tukey, J. W. 1972, *Robust Estimates of Location: Survey and Advances*, (Princeton, Princeton University)
 Basu, S. & Rana, N. C. 1992, *ApJ*, 393, 373.

- Beers, T. C., Flynn, K., & Gebhardt, K. 1990, *AJ*, 100, 32
- Bertelli, G., Bressan, A., Chiosi, C., Fagotto, F. & Nasi, E. 1994, *A&AS* 106, 275.
- Bolte, M. 1989, *ApJ*, 341, 168.
- Burkert, A., Brown, J., & Truran, J. W. 1993, in “The Globular Cluster-Galaxy Connection” p. 656. ASP Conference Series, 48, eds. G.H. Smith and J.P. Brodie.
- Chernoff, D. F. & Weinberg, M. D. 1990, *ApJ*, 351, 121.
- Djorgovski, S. 1987, in *Globular Cluster Systems in Galaxies*, IAU Symp. No. 126, edited by J. Grindlay and A.G.D. Philip (Reidel, Dordrecht), p. 333
- Elson, R. A. W., Fall, S. M., & Freeman, K. C. 1989a, *ApJ*, 336, 734
- Elson, R. A. W., Freeman, K. C., & Lauer, T. R. 1989b, *ApJ*, 347, 69.
- Elson, R. A. W. 1991, *ApJS*, 76, 185.
- Hertz, P., & Grindlay, J. E. 1985, *ApJ*, 298, 95
- Holtzman, J. A. et al. 1995, *PASP*, 107, 1065.
- Hunter, D. A., Light, R. M., Holtzman, J. A., Lynds, R., O’Neil, E., & Grillmair, C. J. 1997, *ApJ*, 478, 124.
- Hunter, D. A., Shaya, E. J., Holtzman, J. A., Light, R. M., O’Neil, E. J., Jr., & Lynds, R. 1995, *ApJ*, 448, 179
- Inagaki, S. & Saslaw, W. C. 1985, *ApJ*, 292, 339.
- King, I. R. 1966, *AJ*, 71, 64.
- Lee, M.–G. 1990, Ph. D. Thesis, University of Washington
- Lynden-Bell, D. 1967, *MNRAS*, 136, 101
- Mateo M. 1988, *ApJ*, 331, 261
- Mateo, M., Olzewski, E. W. & Madore, B. F. 1990, *ApJ*, 353, L11.
- Mateo, M. 1992, in “The Globular Cluster-Galaxy Connection” p. 387. ASP Conference Series, 48, eds. G.H. Smith and J.P. Brodie.
- Meylan, G., & Heggie, D. C. 1997, *A&A Rev*, 8, 1
- Murray, S. D., & Lin, D. N. C. 1996, *ApJ*, 467, 728.
- Murray, S. D., & Lin, D. N. C. 1993, in “The Globular Cluster-Galaxy Connection” p. 738. ASP Conference Series, 48, eds. G.H. Smith and J.P. Brodie.
- Papenhausen, P. 1994, Ph. D. Thesis, Rutgers, the State University of New Jersey.
- Podsiadlowski, P. & Price, N. M. 1992, *Nature*, 359, 305.

Pryor, C., McClure, R. D., Fletcher, J. M. & Hesser, J. E. 1989, *AJ*, 98, 596.

Sagar, R. & Richtler, T. 1991, *A&A*, 250, 324.

Shu, F. H., Adams, F. C., Lizano, S. 1987, *ARA&A*, 25, 23.

Spitzer, L. 1969, *ApJ*, 158, L139

Stetson, P. B. 1987, *PASP*, 99, 191.

Stetson, P. B., Davis, L. E. & Crabtree, D. R. 1990, in *CCDs in Astronomy*, ed. G. H. Jacoby, ASP Conf. Ser., 8, 289–304.

Table 9. Luminosity Functions

Mag ¹	Inner Region		Intermediate Region		Outer Region	
	N _V	N _I	N _V	N _I	N _V	N _I
16.38	24 ± 10	12 ± 7	12 ± 7	8 ± 6	16 ± 8	12 ± 8
16.62	47 ± 13	40 ± 13	20 ± 9	4 ± 4	24 ± 10	12 ± 8
16.88	67 ± 16	47 ± 13	24 ± 10	20 ± 9	40 ± 13	24 ± 10
17.12	74 ± 16	73 ± 16	47 ± 13	39 ± 12	20 ± 11	28 ± 12
17.38	73 ± 16	73 ± 16	53 ± 15	39 ± 12	56 ± 16	44 ± 14
17.62	94 ± 18	87 ± 18	58 ± 15	64 ± 16	84 ± 18	56 ± 16
17.88	142 ± 23	95 ± 18	69 ± 17	62 ± 15	88 ± 19	83 ± 19
18.12	154 ± 24	155 ± 24	101 ± 20	76 ± 18	83 ± 19	88 ± 19
18.38	146 ± 23	155 ± 24	94 ± 19	99 ± 19	88 ± 20	79 ± 19
18.62	230 ± 30	182 ± 26	101 ± 20	93 ± 19	126 ± 24	97 ± 22
18.88	279 ± 34	237 ± 30	175 ± 26	132 ± 23	130 ± 25	122 ± 24
19.12	205 ± 29	272 ± 33	129 ± 23	186 ± 27	227 ± 32	243 ± 32
19.38	256 ± 34	220 ± 30	177 ± 26	145 ± 23	230 ± 32	241 ± 34
19.62	268 ± 34	335 ± 38	193 ± 28	262 ± 32	154 ± 29	154 ± 30
19.88	333 ± 39	345 ± 38	231 ± 31	191 ± 27	300 ± 39	259 ± 39
20.12	293 ± 36	349 ± 39	239 ± 31	277 ± 34	254 ± 38	340 ± 46
20.38	282 ± 37	347 ± 39	319 ± 38	336 ± 38	320 ± 43	416 ± 49
20.62	345 ± 40	434 ± 46	243 ± 33	321 ± 38	274 ± 42	423 ± 53
20.88	326 ± 41	520 ± 53	208 ± 31	311 ± 38	403 ± 49	456 ± 60
21.12	317 ± 39	395 ± 48	194 ± 30	286 ± 38	262 ± 46	376 ± 60
21.38	271 ± 38	441 ± 52	193 ± 30	326 ± 41	305 ± 50	381 ± 65
21.62	218 ± 35	312 ± 42	209 ± 31	338 ± 41	275 ± 55	506 ± 65
21.88	356 ± 46	384 ± 50	232 ± 35	242 ± 35	342 ± 61	480 ± 67
22.12	283 ± 40	356 ± 51	259 ± 35	394 ± 45	430 ± 60	416 ± 70
22.38	311 ± 43	386 ± 58	247 ± 35	357 ± 46	355 ± 61	426 ± 79
22.62	255 ± 42	411 ± 60	287 ± 39	253 ± 39	384 ± 66	553 ± 82
22.88	308 ± 50	291 ± 55	294 ± 40	374 ± 48	402 ± 73	376 ± 84
23.12	353 ± 52	373 ± 63	232 ± 37	376 ± 54	454 ± 75	582 ± 88
23.38	342 ± 56	415 ± 81	304 ± 43	346 ± 55	393 ± 77	546 ± 97
23.62	265 ± 50	315 ± 73	298 ± 44	353 ± 57	278 ± 79	417 ± 93
23.88	355 ± 62	348 ± 102	330 ± 49	358 ± 72	393 ± 80	803 ± 15
24.12	349 ± 69	198 ± 85	232 ± 42	284 ± 71	430 ± 85	734 ± 110
24.38	164 ± 52	837 ± 289	256 ± 47	406 ± 139	399 ± 88	927 ± 130
24.62	297 ± 79	...	194 ± 46	...	453 ± 90	1126 ± 172

Table 9—Continued

Mag ¹	Inner Region		Intermediate Region		Outer Region	
	N _V	N _I	N _V	N _I	N _V	N _I
24.88	237 ± 89	...	404 ± 83	...	306 ± 97	2051 ± 347
25.12	359 ± 132	...	238 ± 66	...	322 ± 94	...
25.38	732 ± 272	...	247 ± 91	...	309 ± 92	...
25.62	276 ± 110	...
25.88	633 ± 163	...

¹Magnitudes are dereddened assuming E(B–V)=0.1

Table 10. Power-law Indices

Region	x_V	χ^2_ν	x_I	χ^2_ν
Inner	0.80 ± 0.40	1.37	0.80 ± 0.35	1.32
Intermediate	1.10 ^{+0.45} _{-0.40}	0.92	1.15 ^{+0.40} _{-0.35}	1.66
Outer	1.30 ± 0.45	1.53	1.50 ± 0.40	1.83

Table 11. χ^2 Test Results.

Samples Compared	V-band				I-band			
	V_{lim}	χ^2_ν	ν	$P(\chi^2)$	I_{lim}	χ^2_ν	ν	$P(\chi^2)$
inner	25	1.34	34	0.09	24	1.60	30	0.02
<i>vs.</i>	24	1.20	30	0.21	23	1.62	26	0.02
intermed.	23	1.17	26	0.25	22	1.22	22	0.21
	22	0.96	22	0.52	21	1.10	18	0.34
inner	25	2.16	34	< 0.01	24	2.75	30	< 0.01
<i>vs.</i>	24	2.10	30	< 0.01	23	2.42	26	< 0.01
outer	23	2.26	26	< 0.01	22	2.46	22	< 0.01
	22	1.88	22	0.01	21	2.01	18	< 0.01
intermed.	25	1.26	34	0.15	24	1.40	30	0.07
<i>vs.</i>	24	1.16	30	0.21	23	1.34	26	0.11
outer	23	1.16	26	0.25	22	1.24	22	0.20
	22	1.12	22	0.32	21	1.12	18	0.32

TABLE 12. KS Statistic Results.

Samples Compared	V-band Luminosity Functions							I-band Luminosity Functions						
	V_{lim}	N_i	N_o	N_b	KS Stat.	V_{KS}	Frac. > obs.	I_{lim}	N_i	N_o	N_b	KS Stat.	I_{KS}	Frac. > obs.
inner	25	1534	1429	2291	0.0792	21.42	0.0043	24	1529	1424	2218	0.0803	21.33	0.0039
vs.	24	1464	1291	1547	0.0705	21.36	0.0049	23	1420	1233	1344	0.0694	21.32	0.0064
intermed.	23	1296	1062	884	0.0696	20.21	0.0111	22	1230	946	654	0.0595	19.62	0.0430
	22	1100	815	438	0.0576	19.20	0.0869	21	952	671	252	0.0652	19.59	0.0630
inner	25	1534	4129	2291	0.1122	21.63	0.0010	24	1529	4023	2218	0.1106	21.46	0.0013
vs.	24	1464	3181	1547	0.1047	20.38	0.0015	23	1420	2868	1344	0.0945	19.98	0.0060
outer	23	1296	2234	884	0.1144	20.21	0.0001	22	1230	1847	654	0.0976	19.98	0.0059
	22	1100	1433	438	0.0937	18.95	0.0171	21	952	1037	252	0.0885	19.13	0.0517
intermed.	25	1429	4129	2291	0.0523	20.77	0.2989	24	1424	4023	2218	0.0393	20.68	0.6273
vs.	24	1291	3181	1547	0.0542	20.77	0.2505	23	1233	2868	1344	0.0399	22.78	0.6238
outer	23	1062	2234	884	0.0670	20.77	0.0974	22	946	1847	654	0.0552	20.64	0.2675
	22	815	1433	438	0.0588	20.77	0.2793	21	671	1037	252	0.0462	19.94	0.6391

Table 13. V -band Surface Brightness Profile.

$\log(r)$ (arcsec)	SB ¹ (mag arcsec ⁻²)	$\log(r)$ (arcsec)	SB (mag arcsec ⁻²)
-0.137	17.13 ± 0.06	2.177	20.16 ± 0.01
0.131	17.15 ± 0.09	2.231	20.17 ± 0.02
0.254	17.23 ± 0.09	2.279	20.15 ± 0.01
0.353	17.29 ± 0.09	2.323	20.17 ± 0.01
0.450	17.37 ± 0.10	2.362	20.17 ± 0.02
0.551	17.36 ± 0.10	2.398	20.16 ± 0.04
0.654	17.34 ± 0.16	2.432	20.16 ± 0.01
0.757	17.33 ± 0.27	2.463	20.16 ± 0.01
0.857	17.69 ± 0.37	2.492	20.16 ± 0.02
0.957	17.85 ± 0.22	2.519	20.15 ± 0.02
1.057	18.01 ± 0.32	2.545	20.18 ± 0.02
1.156	18.16 ± 0.12	2.569	20.16 ± 0.14
1.256	18.73 ± 0.16	2.591	20.17 ± 0.07
1.357	19.16 ± 0.11	2.613	20.13 ± 0.07
1.457	19.69 ± 0.09	2.633	19.99 ± 0.08
1.557	19.82 ± 0.07	2.653	20.05 ± 0.09
1.657	20.02 ± 0.04	2.672	20.14 ± 0.20
1.757	20.07 ± 0.01	2.690	20.16 ± 0.28
1.857	20.10 ± 0.03	2.708	19.97 ± 0.24
1.955	20.10 ± 0.07	2.724	20.17 ± 0.38
2.042	20.16 ± 0.06	2.739	20.14 ± 0.45
2.114	20.17 ± 0.04		

¹Background level is $V = 20.16 \pm 0.005$

Table 1. Luminosity Functions

Mag ¹	Inner Region		Intermediate Region		Outer Region	
	N _V	N _I	N _V	N _I	N _V	N _I
16.38	24 ± 10	12 ± 7	12 ± 7	8 ± 6	16 ± 8	12 ± 8
16.62	47 ± 13	40 ± 13	20 ± 9	4 ± 4	24 ± 10	12 ± 8
16.88	67 ± 16	47 ± 13	24 ± 10	20 ± 9	40 ± 13	24 ± 10
17.12	74 ± 16	73 ± 16	47 ± 13	39 ± 12	20 ± 11	28 ± 12
17.38	73 ± 16	73 ± 16	53 ± 15	39 ± 12	56 ± 16	44 ± 14
17.62	94 ± 18	87 ± 18	58 ± 15	64 ± 16	84 ± 18	56 ± 16
17.88	142 ± 23	95 ± 18	69 ± 17	62 ± 15	88 ± 19	83 ± 19
18.12	154 ± 24	155 ± 24	101 ± 20	76 ± 18	83 ± 19	88 ± 19
18.38	146 ± 23	155 ± 24	94 ± 19	99 ± 19	88 ± 20	79 ± 19
18.62	230 ± 30	182 ± 26	101 ± 20	93 ± 19	126 ± 24	97 ± 22
18.88	279 ± 34	237 ± 30	175 ± 26	132 ± 23	130 ± 25	122 ± 24
19.12	205 ± 29	272 ± 33	129 ± 23	186 ± 27	227 ± 32	243 ± 32
19.38	256 ± 34	220 ± 30	177 ± 26	145 ± 23	230 ± 32	241 ± 34
19.62	268 ± 34	335 ± 38	193 ± 28	262 ± 32	154 ± 29	154 ± 30
19.88	333 ± 39	345 ± 38	231 ± 31	191 ± 27	300 ± 39	259 ± 39
20.12	293 ± 36	349 ± 39	239 ± 31	277 ± 34	254 ± 38	340 ± 46
20.38	282 ± 37	347 ± 39	319 ± 38	336 ± 38	320 ± 43	416 ± 49
20.62	345 ± 40	434 ± 46	243 ± 33	321 ± 38	274 ± 42	423 ± 53
20.88	326 ± 41	520 ± 53	208 ± 31	311 ± 38	403 ± 49	456 ± 60
21.12	317 ± 39	395 ± 48	194 ± 30	286 ± 38	262 ± 46	376 ± 60
21.38	271 ± 38	441 ± 52	193 ± 30	326 ± 41	305 ± 50	381 ± 65
21.62	218 ± 35	312 ± 42	209 ± 31	338 ± 41	275 ± 55	506 ± 65
21.88	356 ± 46	384 ± 50	232 ± 35	242 ± 35	342 ± 61	480 ± 67
22.12	283 ± 40	356 ± 51	259 ± 35	394 ± 45	430 ± 60	416 ± 70
22.38	311 ± 43	386 ± 58	247 ± 35	357 ± 46	355 ± 61	426 ± 79
22.62	255 ± 42	411 ± 60	287 ± 39	253 ± 39	384 ± 66	553 ± 82
22.88	308 ± 50	291 ± 55	294 ± 40	374 ± 48	402 ± 73	376 ± 84
23.12	353 ± 52	373 ± 63	232 ± 37	376 ± 54	454 ± 75	582 ± 88
23.38	342 ± 56	415 ± 81	304 ± 43	346 ± 55	393 ± 77	546 ± 97
23.62	265 ± 50	315 ± 73	298 ± 44	353 ± 57	278 ± 79	417 ± 93
23.88	355 ± 62	348 ± 102	330 ± 49	358 ± 72	393 ± 80	803 ± 15
24.12	349 ± 69	198 ± 85	232 ± 42	284 ± 71	430 ± 85	734 ± 110
24.38	164 ± 52	837 ± 289	256 ± 47	406 ± 139	399 ± 88	927 ± 130
24.62	297 ± 79	...	194 ± 46	...	453 ± 90	1126 ± 172

Table 1—Continued

Mag ¹	Inner Region		Intermediate Region		Outer Region	
	N _V	N _I	N _V	N _I	N _V	N _I
24.88	237 ± 89	...	404 ± 83	...	306 ± 97	2051 ± 347
25.12	359 ± 132	...	238 ± 66	...	322 ± 94	...
25.38	732 ± 272	...	247 ± 91	...	309 ± 92	...
25.62	276 ± 110	...
25.88	633 ± 163	...

¹Magnitudes are dereddened assuming E(B–V)=0.1

TABLE 10. Power-law Indices

Region	x_V	χ^2_ν	x_I	χ^2_ν
Inner	0.80 ± 0.40	1.37	0.80 ± 0.35	1.32
Intermediate	$1.10^{+0.45}_{-0.40}$	0.92	$1.15^{+0.40}_{-0.35}$	1.66
Outer	1.30 ± 0.45	1.53	1.50 ± 0.40	1.83

TABLE 11. χ^2 Test Results.

Samples Compared	V-band				I-band			
	V_{lim}	χ^2_ν	ν	$P(\chi^2)$	I_{lim}	χ^2_ν	ν	$P(\chi^2)$
inner	25	1.34	34	0.09	24	1.60	30	0.02
<i>vs.</i>	24	1.20	30	0.21	23	1.62	26	0.02
intermed.	23	1.17	26	0.25	22	1.22	22	0.21
	22	0.96	22	0.52	21	1.10	18	0.34
inner	25	2.16	34	< 0.01	24	2.75	30	< 0.01
<i>vs.</i>	24	2.10	30	< 0.01	23	2.42	26	< 0.01
outer	23	2.26	26	< 0.01	22	2.46	22	< 0.01
	22	1.88	22	0.01	21	2.01	18	< 0.01
intermed.	25	1.26	34	0.15	24	1.40	30	0.07
<i>vs.</i>	24	1.16	30	0.21	23	1.34	26	0.11
outer	23	1.16	26	0.25	22	1.24	22	0.20
	22	1.12	22	0.32	21	1.12	18	0.32

TABLE 13. *V*-band Surface Brightness Profile.

$\log(r)$ (arcsec)	SB ¹ (mag arcsec ⁻²)	$\log(r)$ (arcsec)	SB (mag arcsec ⁻²)
-0.137	17.13 ± 0.06	2.177	20.16 ± 0.01
0.131	17.15 ± 0.09	2.231	20.17 ± 0.02
0.254	17.23 ± 0.09	2.279	20.15 ± 0.01
0.353	17.29 ± 0.09	2.323	20.17 ± 0.01
0.450	17.37 ± 0.10	2.362	20.17 ± 0.02
0.551	17.36 ± 0.10	2.398	20.16 ± 0.04
0.654	17.34 ± 0.16	2.432	20.16 ± 0.01
0.757	17.33 ± 0.27	2.463	20.16 ± 0.01
0.857	17.69 ± 0.37	2.492	20.16 ± 0.02
0.957	17.85 ± 0.22	2.519	20.15 ± 0.02
1.057	18.01 ± 0.32	2.545	20.18 ± 0.02
1.156	18.16 ± 0.12	2.569	20.16 ± 0.14
1.256	18.73 ± 0.16	2.591	20.17 ± 0.07
1.357	19.16 ± 0.11	2.613	20.13 ± 0.07
1.457	19.69 ± 0.09	2.633	19.99 ± 0.08
1.557	19.82 ± 0.07	2.653	20.05 ± 0.09
1.657	20.02 ± 0.04	2.672	20.14 ± 0.20
1.757	20.07 ± 0.01	2.690	20.16 ± 0.28
1.857	20.10 ± 0.03	2.708	19.97 ± 0.24
1.955	20.10 ± 0.07	2.724	20.17 ± 0.38
2.042	20.16 ± 0.06	2.739	20.14 ± 0.45
2.114	20.17 ± 0.04		

¹Background level is $V = 20.16 \pm 0.005$